

# Ground Motion Model for Small-to-Moderate Earthquakes in Texas, Oklahoma, and Kansas

Georgios Zalachoris,<sup>a)</sup> and Ellen M. Rathje,<sup>a)</sup> M.EERI

A ground motion model (GMM) tuned to the characteristics of the observed, and potentially induced, seismicity in Texas, Oklahoma, and Kansas is developed using a database of 4,528 ground motions recorded during 376 events of  $M_w > 3.0$  in the region. The GMM is derived using the referenced empirical approach with an existing Central and Eastern North America model as the reference GMM and is applicable for  $M_w = 3.0$ – $5.8$  and hypocentral distances less than 500 km. The proposed model incorporates weaker magnitude scaling than the reference GMM for periods less than about 1.0 s, resulting in smaller predicted ground motions at larger magnitudes. The proposed model predicts larger response spectral accelerations at short hypocentral distances ( $\leq 20$  km), which is likely because of the shallow hypocenters of events in Texas, Oklahoma, and Kansas. Finally, the  $V_{S30}$  scaling for the newly developed model predicts less amplification at  $V_{S30} < 600$  m/s than the reference GMM, which is likely because of the generally thinner sediments in the study area. This finding is consistent with recent studies regarding site amplification in Central and Eastern North America. [DOI: 10.1193/022618EQS047M]

## INTRODUCTION

The Central and Eastern United States have seen an increase in seismicity over the last 10 years (Ellsworth 2013), with the seismicity rates in some regions (e.g., North Texas/Oklahoma/South Kansas) increasing by more than an order of magnitude (Petersen et al. 2016). The increased seismicity has been associated with human activities, such as fluid injection or extraction (Ellsworth 2013, Hough 2014). These potentially induced earthquakes nucleate as a result of increased pore pressure from processes like waste water injection and release stored tectonic stress along an adjacent fault (Hough 2014).

The observed increase in seismicity has made the evaluation of the seismic hazard in these regions increasingly pertinent, which requires the development of ground motion models (GMMs) that are tuned to the characteristics of the observed, and potentially induced, seismicity. Because of their nature, induced events are likely to be of smaller magnitude and at shallower focal depth than natural earthquakes. The focal depths of potentially induced events generally lie within the upper 5 km of the crust, making the seismic wave propagation more dependent on the heterogeneous properties of the uppermost crustal layers (Bommer et al. 2016). Therefore, GMMs developed for regions with potentially induced events should

---

<sup>a)</sup> Department of Civil, Architectural, and Environmental Engineering, University of Texas, Austin, TX 78712; Email: e.rathje@mail.utexas.edu (E. M. R.)

focus on providing robust predictions for smaller, shallow earthquakes at close source-to-site distances (Douglas et al. 2013). These characteristics of induced seismicity often make the development of application-specific or region-specific GMMs a necessity.

Accordingly, Atkinson (2015, APIE15) developed a GMM for small-to-moderate earthquake events at short hypocentral distances with application to regions with induced seismicity. Atkinson (2015) used recorded data from California for events with  $M_w = 3-6$  and hypocentral distances less than 40 km and noted that the use of hypocentral distance as a distance metric is better suited for such applications because it allows for a functional form of GMM that correctly reflects the point source scaling attributes that apply to small-to-moderate events. Atkinson (2015) recognized that because of shallow focal depths, which bring the events very close to the epicenter, the ground motions from small-to-moderate induced events at short distances may be significantly larger than those predicted by most current GMM. Nonetheless, it was also concluded that the vicinity of the source to the surface may be partially counteracted by the tendency of shallow events to have lower stress drops.

The present study takes advantage of recordings at seismic stations in Texas, Oklahoma, and Kansas to develop a new GMM for small-to-moderate earthquake events particularly tuned to the characteristics of the observed, and potentially induced, seismicity in these states. Given that the recordings in the region are too sparse within the magnitude-distance ranges of engineering interest to allow direct development of GMMs by empirical regression techniques and acknowledging the generic similarities in anelastic attenuation and geometrical spreading characteristics (at least in regional distances) between potentially induced events and natural seismicity (Atkinson 2015), the new model is developed using the referenced empirical approach (Atkinson 2008) with the Hassani and Atkinson (2015, HA15) Central and Eastern North America (CENA) model as the reference GMM. The Hassani and Atkinson (2015) model was developed as part of the NGA-East project (Pacific Earthquake Engineering Research Center 2015) and was itself developed by updating the Western North America (WNA) GMM of Boore et al. (2014) using the referenced empirical approach. Thus the approach adopted here aims to take advantage of the knowledge accumulated based on recorded ground motion amplitude data from both WNA and CENA regarding important but complex source and distance scaling effects.

## GROUND MOTION DATABASE FOR TEXAS, OKLAHOMA, AND KANSAS

Currently, there is not a complete, consistently processed, and widely utilized ground motion database for potentially induced earthquakes in Texas, Oklahoma, and Kansas. Therefore, following the general event selection and signal processing framework adopted by the NGA-East project (Goulet et al. 2014), recordings at seismic stations in Texas, Oklahoma, and Kansas were used to develop a database of the following ground motion intensity measures (IMs): peak ground acceleration (PGA), peak ground velocity (PGV), and response spectral acceleration (5% damped pseudo-acceleration, PSA) at spectral periods from 0.05 to 10 s for horizontal components of shaking.

To obtain a substantial number of earthquake ground motions, a catalog of earthquake events with epicenters located in Texas, Oklahoma, and Kansas was created. For that purpose, the comprehensive database of the Incorporated Research Institutions for Seismology,

IRIS (2018), was utilized. Accordingly, 376 earthquake events occurring between January 2005 and November 2016 with magnitudes greater than 3.0 and at least 3 ground motion recordings were selected. Because of the inherent difficulty in separating mainshock and aftershock events during the swarms of potentially induced earthquakes in the region, the events included in the database are not distinguished as mainshocks and aftershocks. The locations of the selected earthquakes are illustrated in Figure 1a. Figure 1b shows the locations of the seismic stations in Texas, Oklahoma and Kansas that recorded ground motion data during the events shown in Figure 1a. Because of the substantially different geologic characteristics of the Gulf Coast Plain and the associated difference in site amplification, the ground motion data recorded at seismic stations located within the Gulf Coast Plain (Figure 1b) are not considered in this study.

The moment magnitudes ( $M_w$ ) of the selected earthquakes were either known through IRIS or computed using 1-Hz PSA amplitudes of the vertical component of the ground motion records (Atkinson and Mahani 2013, Atkinson et al. 2014). The 1-Hz PSA method uses a semiempirical relationship to compute  $M_w$  from the recorded vertical 1-Hz PSA and site-to-source distance and is based on the fact that at  $M_w$  less than about 4, the motion at 1-Hz is directly proportional to the seismic moment. The 1-Hz PSA method was primarily used for events with  $M_w \leq 4.0$ . To obtain a certain degree of validation for the utilized  $M_w$  estimates, Figure 2 presents a comparison of the  $M_w$  values reported by IRIS and those estimated using the 1-Hz PSA method for earthquake events with  $M_w \leq 4.5$ , where both values were available. Based on Figure 2, it can be concluded that the 1-Hz PSA method reproduces

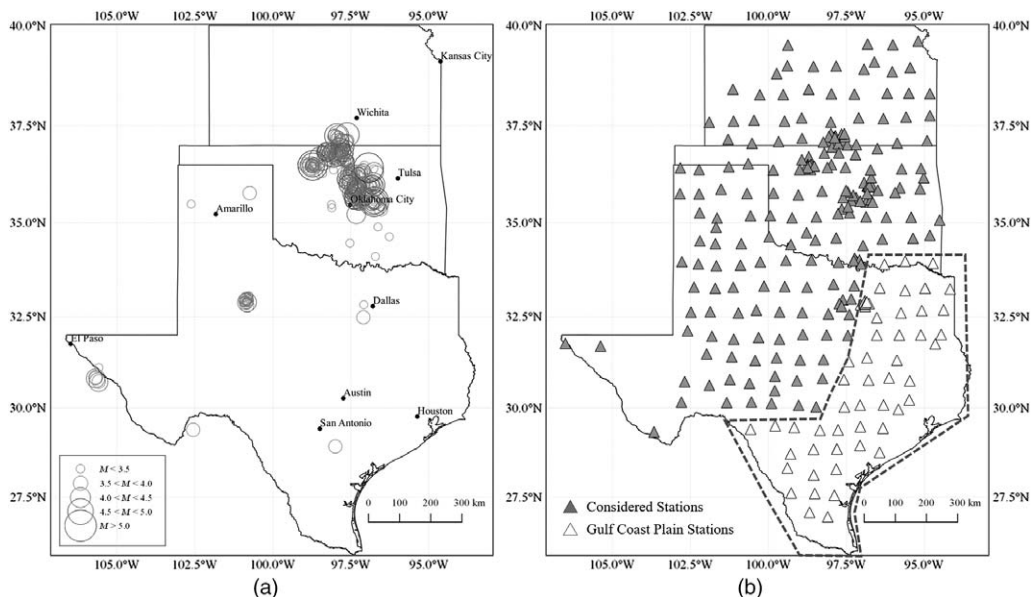


**Figure 1.** Map of the states of Texas, Oklahoma, and Kansas showing (a) locations of earthquake epicenters of the selected events and (b) locations of seismic stations considered in this study.

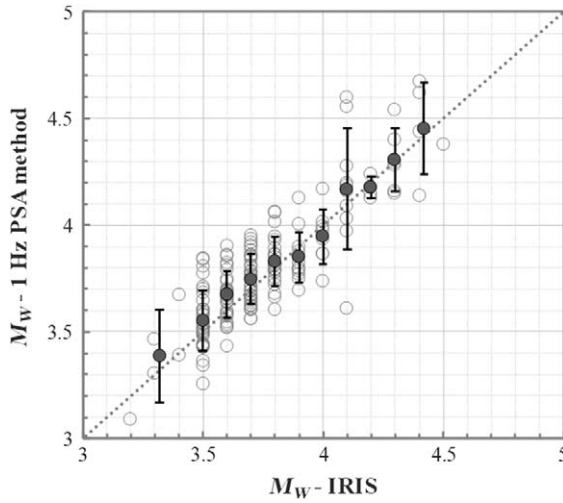


**Figure 2.** Comparison between  $M_w$  values computed based on 1-Hz PSA amplitudes of the vertical component of the ground motion records (Atkinson and Mahani 2013, Atkinson et al. 2014) with the ones reported by IRIS for events with  $M_w \leq 4.5$ . Mean values and  $\pm 1\sigma$  error bars are also depicted.

the  $M_w$  values reported by IRIS relatively accurately and can be used for events where  $M_w$  is not available. Accordingly, 201 of the 376 events had their  $M_w$  values assigned using the 1-Hz PSA method.

Ground motion data recorded at the stations in Figure 1b were retrieved using tools available via IRIS (i.e., Standing Order for Data). The collected data and associated metadata were quality assured and reviewed several times. All collected time series were processed in a unified manner. The recordings were instrument-corrected and the mean was removed. The records were examined for obvious irregularities (i.e., clipping, distortion, apparent high noise) on an individual basis. Then 5% cosine tapering, acausal Butterworth filtering, and baseline correction were applied. The high-pass and low-pass filter frequencies were determined based on a Signal-to-Noise Ratio (SNR) threshold of 3. Any records with SNR values consistently less than 3 within the examined bandwidth were rejected. Overall, the developed ground motion database consists of 4,528 three-component ground motion records from 213 seismic stations. Finally, rotation-angle-independent ground motion IMs (RotD50, Boore 2010) were computed for 429 spectral periods, as per the NGA-East database (Goulet et al. 2014).

To quantify site amplification, most GMMs use the time-averaged shear wave velocity of the upper 30 m (i.e.,  $V_{S30}$ ) as a measure of the physical properties of the near-surface geologic conditions. Because of the lack of existing in-situ measurements of shear wave velocity profiles in Texas, Oklahoma, and Kansas, reliable proxy estimates of  $V_{S30}$  values in these states are necessary. An approach to developing  $V_{S30}$  estimates at seismic station locations is the  $P$ -wave seismogram method (Ni and Somerville 2014, Kim et al. 2016),

which uses recordings from seismic stations and theoretical wave propagation considerations to estimate  $V_{S30}$ . [Zalachoris et al. \(2017\)](#) used the  $P$ -wave seismogram method to estimate  $V_{S30}$  at 251 seismic station locations in Texas, Oklahoma, and Kansas. Furthermore, the relationship between the  $V_{S30}$  estimates and geologic conditions at the locations of each site, as documented by large-scale geologic maps, was investigated. As a result, [Zalachoris et al. \(2017\)](#) developed a geology-based proxy method that uses geologic age and lithology to assign  $V_{S30}$  values to locations where neither in-situ measurements nor  $P$ -wave seismogram estimates of shear wave velocity are available. Further study of the data from [Zalachoris et al. \(2017\)](#), as detailed in [Cox et al. \(2017\)](#), indicated statistically significant differences between the  $V_{S30}$  of the Quaternary units along the Gulf Coast and the Quaternary units outside the Gulf Coast region. The revised geology-based protocol for proxy assignment of  $V_{S30}$  values in Texas (excluding the Gulf Coast Plain), Oklahoma, and Kansas is shown in Table 1. In this study, the preferred method to assign  $V_{S30}$  to stations was field measurements. If field measurements were not available,  $V_{S30}$  values estimated by the  $P$ -wave seismogram method, as reported by [Zalachoris et al. \(2017\)](#), were used. Finally, if neither field measurements or  $P$ -wave seismogram estimates were not available, proxy-based  $V_{S30}$  values from Table 1 were utilized. Of the 213 seismic stations with recordings in the ground motion database, two had in-situ measurements of  $V_{S30}$ , 198 were assigned  $V_{S30}$  from the  $P$ -wave seismogram approach, and 14 were assigned  $V_{S30}$  from the geology-based proxy method using the statewide geologic maps of surface geology, as described in [Zalachoris et al. \(2017\)](#).

**Table 1.** Geology-based protocol for  $V_{S30}$  proxy assignment from [Cox et al. \(2017\)](#) based on data from [Zalachoris et al. \(2017\)](#)

Geologic age	Rock type	$N_{pts}$	$V_S$ (m/s)	$\sigma_{\ln V}$
Quaternary (Holocene)	Alluvium and terrace deposits	5	544	0.31
Quaternary (Pleistocene)	Alluvium and terrace deposits; clay, silt, and loess; sand and gravel	33	447	0.62
Quaternary (undivided)	Alluvium and terrace deposits; clay, silt, and loess; sand and gravel	17	540	0.53
Tertiary	Clay, silt, and loess	13	349	0.25
	Sand and gravel; mudstone, claystone, siltstone, sandstone, conglomerate, marl, and shale	28	478	0.3
	Chert, basalt, granite, and rhyolite	1	1,077	N/A
Mesozoic	Sand and gravel; mudstone, claystone, siltstone, sandstone, conglomerate, marl, and shale	29	543	0.41
	Limestone, chalk, and evaporite	20	727	0.37
Paleozoic	Mudstone, claystone, siltstone, sandstone, conglomerate, marl, and shale	74	756	0.39
	Limestone, chalk, and evaporite	12	981	0.27
Paleozoic/Precambrian	Chert, basalt, granite, and rhyolite	5	1,519	0.06

Note: Only data outside the Gulf Coast Plain are considered.  $N_{pts}$ , number of data points;  $V_S$ , median  $V_S$  for the group;  $\sigma_{\ln V}$ , standard deviation of the natural log of the  $V_S$  for the group.

To assess the accuracy of both the  $P$ -wave seismogram  $V_{S30}$  estimates and geology-based  $V_{S30}$  proxies, we compare them with  $V_{S30}$  values derived from a series of in-situ  $V_S$  measurements (Figure 3) recently performed at seismic station locations in the Dallas–Fort Worth area using a combination of linear array active-source and two-dimensional array ambient-wavefield surface wave testing by Cox et al. (2017). These seismic station locations coincide with locations where  $P$ -wave seismogram estimates were available by Zalachoris et al. (2017). Also shown is the measured  $V_{S30}$  at the Wichita Mountains seismic station (US.WMOK) in Oklahoma ( $V_{S30} = 1,859$  m/s, Yong et al. 2015), located on Paleozoic granite. In Figure 3, error bars ( $\pm 1$  standard deviation) for the  $V_{S30}$  values are shown. For the in-situ measurements, the error bars represent the  $\pm 1$  standard deviation reported from the surface wave inversions of shear wave velocity; for the  $P$ -wave seismogram values, the error bars represent the  $\pm 1$  standard deviation of the  $V_{S30}$  values computed from individual records; and for the geology-based proxy values, the error bars represent  $\pm 1$  standard deviation of the  $V_{S30}$  values for the corresponding geologic age/lithology group (Zalachoris et al. 2017).

For the  $P$ -wave seismogram method as compared with the measurements (Figure 3a), the mean bias ( $\ln(V_{S30,measured}/V_{S30,estimated})$ ) is on the order of 0.1, which translates to an average underprediction of the  $V_{S30}$  values by 10%. Similarly, the geology-based proxy method (Table 1) also compares favorably with the in-situ measured  $V_{S30}$  values (Figure 3b), with a mean bias on the order of  $-0.1$  corresponding to an average overprediction of the  $V_{S30}$  values by 10%. The standard deviations of the computed bias are  $\sigma_{ln} = 0.30$  for the  $P$ -wave seismogram method and  $\sigma_{ln} = 0.25$  for the geology-based proxy. Because the geology-based proxy method assigns the same  $V_{S30}$  value to sites within the same geologic age/lithology group, Figure 3b shows many sites with the same  $V_{S30}$  value. The results in

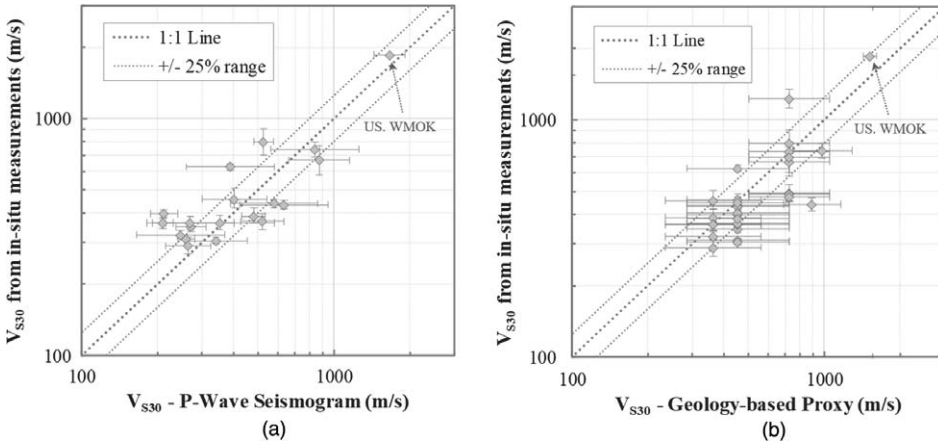


**Figure 3.**  $V_{S30}$  values obtained from in-situ measurements at seismic stations in the Dallas–Fort Worth area (Cox et al. 2017) as compared with  $V_{S30}$  values estimated by the (a)  $P$ -wave seismogram method and (b) geology-based  $V_{S30}$  proxy method.

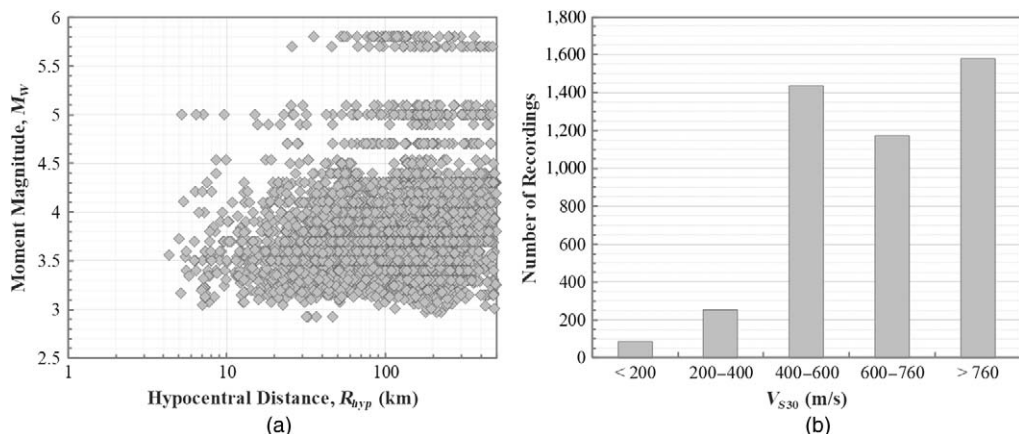


**Figure 4.** Ground motion database utilized in this study: (a) Moment magnitude ( $M_w$ ) and hypocentral distance ( $R_{hyp}$ ) distribution; (b) number of recordings for five  $V_{S30}$  bins.

Figure 3 reveal that  $V_{S30}$  estimates based on the  $P$ -wave seismogram and geology-based proxy methods can be used with confidence at locations where in-situ measurements of  $V_S$  are not available.

Figure 4a illustrates the moment magnitude ( $M_w$ )-hypocentral distance ( $R_{hyp}$ ) coverage of the developed ground motion database, while Figure 4b shows the distribution of the seismic recordings based on their  $V_{S30}$  value. Because of the small magnitudes represented in the database,  $R_{hyp}$  can be taken as equal to the closest distance to the rupture plane (Hassani and Atkinson 2015). Data from events with magnitudes between  $M_w = 3$  and  $M_w = 5.8$  and distances  $R_{hyp} = 4$ – $500$  km are represented in the database, with approximately 856 records with  $R_{hyp} < 50$  km (Figure 4a). The events have a median depth of about 5 km, and 90% of the events have depths less than 7.5 km. In terms of the  $V_{S30}$  distribution of the recordings (Figure 4b), the ground motion database is dominated by stiffer sites with more than 90% of the recordings made at sites with  $V_{S30} > 400$  m/s. Nonetheless, smaller  $V_{S30}$  sites are represented with 85 records from stations with  $V_{S30} < 200$  m/s and 255 records from stations with  $V_{S30}$  between 200 and 400 m/s. The magnitude-distance distribution for this study is similar to the distribution of the data used by Hassani and Atkinson (2015), although Hassani and Atkinson (2015) used epicentral distance and did not report event depths. In terms of the  $V_{S30}$  distribution, the dataset of Hassani and Atkinson (2015) is also dominated by sites with larger  $V_{S30}$ , but it is important to note that they did not use their data to evaluate  $V_{S30}$  scaling.

Figure 5 shows the number of earthquake events (Figure 5a) and ground motion recordings (Figure 5b) included in the database as a function of spectral period for different magnitude ranges. As expected, there is a decrease in available data for periods longer than 2 s, particularly for magnitudes less than  $M_w 3.5$ , which is due to smaller SNR at longer

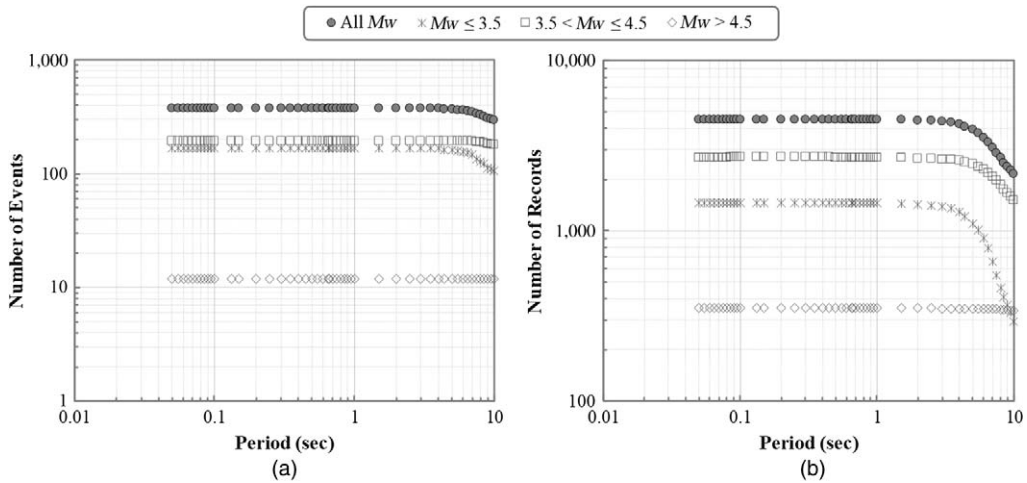


**Figure 5.** (a) Number of earthquake events per spectral period and (b) number of earthquake recordings per spectral period used to develop the GMM.

periods for smaller magnitude events. The full database developed in this study (i.e., event/station information and RotD50 values for each record) is provided in the online Appendices.

### GMM DEVELOPMENT METHOD

We develop a GMM tuned to the seismicity in Texas, Oklahoma, and Kansas by developing adjustment factors for the Hassani and Atkinson (2015) NGA-East GMM using the regional ground motion database described previously. The HA15 GMM is a referenced empirical model that used ground motion data from CENA to adjust the well-calibrated empirical WNA GMM by Boore et al. (2014, BSSA14). In this manner, we make use of region-specific empirical ground-motion data, experience regarding attenuation characteristics from CENA, and an empirical GMM from data-rich WNA to develop an empirical GMM for small-to-moderate earthquakes in Texas, Oklahoma, and Kansas.

To establish the adjustment factors, we compute the residuals, defined as the difference (in natural logarithm units) between the regional observed RotD50 ground motion IMs and the corresponding predicted IMs by the HA15 model. Input parameters for the HA15 model are earthquake magnitude ( $M_w$ ), epicentral distance ( $R_{epi}$ ), site parameter  $V_{S30}$ , and source mechanism (assumed as unspecified). To account for site conditions different than the reference site (i.e.,  $V_{S30} = 760$  m/s), the HA15 model utilizes the BSSA14 site amplification model, which was developed from WNA data.

The total residuals,  $\ln Y_{i,j}$ , are computed for each recording  $j$  and event  $i$  for each  $IM$  as follows:

$$\ln Y_{i,j} = \ln (IM_{obs})_{i,j} - \ln (IM_{pred})_{i,j} \quad (1)$$

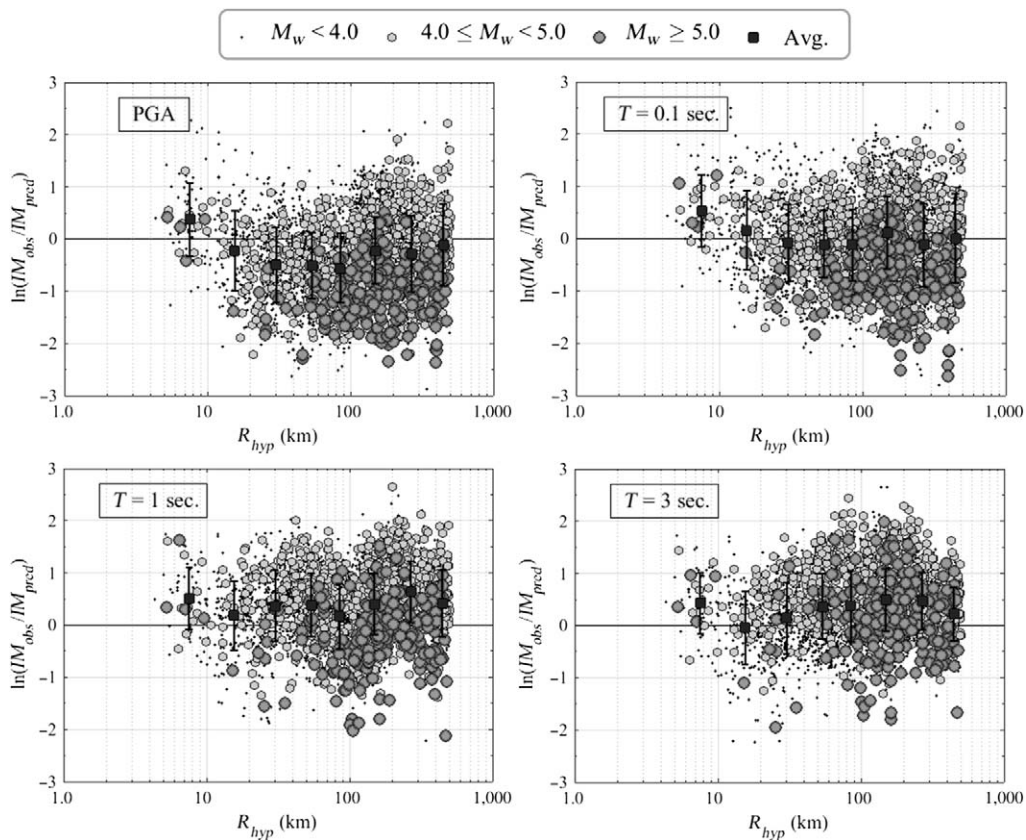


**Figure 6.** Overall residuals ( $\ln Y_{i,j}$ ) at four spectral periods (PGA,  $T = 0.1$ , 1.0, and 3.0 s) versus hypocentral distance ( $R_{hyp}$ ). Data are separated based on three magnitude bins. Mean and  $\pm 1\sigma$  values are depicted for eight log-spaced distance bins (filled squares).

where  $IM_{obs}$  is the observed ground motion  $IM$  and  $IM_{pred}$  is the corresponding predicted value by the HA15 GMM for the given  $M_w$ ,  $R_{epi}$ , and  $V_{S30}$ . Figure 6 presents the variation of the computed overall residuals ( $\ln Y_{i,j}$ ) with hypocentral distance ( $R_{hyp}$ ) at four spectral periods (i.e., PGA,  $T = 0.1$ , 1.0, and 3.0 s). The computed values are separated based on three magnitude bins. From Figure 6, some trends can be readily distinguished: an obvious shift in  $\ln Y_{i,j}$  toward positive values (i.e., observed motions greater than predicted) at  $R_{hyp} < 20$  km and at smaller spectral periods (i.e., PGA,  $T = 0.1$  s) as well as a magnitude dependence of the residuals with more negative residuals (i.e., observed motions smaller than predicted) at larger  $M_w$  for smaller periods and the opposite trend at longer periods.

Using the framework of Hassani and Atkinson (2015), adjustment factors are developed for each spectral period to account for differences in magnitude, distance, and  $V_{S30}$  scaling using the computed total residuals and a mixed-effects regression (Abrahamson and Youngs 1992).

The mixed-effects analysis utilizes the *lme* function in MATLAB to partition the residuals into inter (between)-event and intra (within)-event residuals as follows:

$$\ln Y_{i,j} = C_{adj} + \eta_i + \varepsilon_{i,j} \quad (2)$$

where  $C_{adj}$  is the mean residual representing the average misfit of the reference GMM,  $\eta_i$  is the event term for event  $i$ , and  $\varepsilon_{i,j}$  is the intra-event residual for recording  $j$  and event  $i$ . The event terms ( $\eta_i$ ) are used to develop the adjustments required for the magnitude scaling, while the intra-event residuals ( $\varepsilon_{i,j}$ ) are used to develop the adjustments for distance and  $V_{S30}$  scaling.

The overall adjustment factor ( $F$ ) represents the combined effects of the adjustment factors for magnitude, distance, and  $V_{S30}$  scaling as follows:

$$\ln F = C_{adj} + F_M + F_R + F_S \quad (3)$$

where  $C_{adj}$  is a factor to adjust the overall level of the HA15 model relative to the regional data,  $F_M$  is the adjustment to magnitude scaling,  $F_R$  is the adjustment in the distance scaling, and  $F_S$  is the adjustment to the site amplification model.

To avoid the overlapping influence of the source, distance, and site effects on the mapped residuals, the computation of the adjustment factors is performed using a step-wise iterative approach. First, the adjustment factor for the regional variation in magnitude scaling ( $F_M$ ) is obtained based on a maximum-likelihood regression of the observed magnitude ( $M_w$ ) dependence of the inter-event residuals ( $\eta_i$ ). Then new residuals ( $\ln Y_{i,j}$ ) are computed from Equation 1 using the new magnitude scaling ( $F_M$ ) in the *IM* prediction. A mixed effects analysis of the new residuals provides new intra-event residuals ( $\varepsilon_{i,j}$ ) that are used for the development of adjustment factors for the distance scaling and site amplification model ( $F_R$  and  $F_S$ , respectively) through a maximum-likelihood regression. Again, new residuals are computed from Equation 1, this time using only the new  $F_R$  and  $F_S$  in the *IM* prediction, the residuals are partitioned, and the  $F_M$  relationship is re-evaluated. Iterative estimates of  $F_R$  and  $F_S$  using residuals that incorporate  $F_M$  and estimates of  $F_M$  using residuals that incorporate  $F_R$  and  $F_S$  continue until the models stabilize, typically after less than 5 iterations. The  $p$ -value for each regression coefficient was then computed.

Using the final adjustment factors, the resulting total residuals were partitioned one last time to obtain the overall adjustment factor,  $C_{adj}$  and the inter- and intra-event residuals. Inter-event terms are assumed to be normally distributed with zero mean and standard deviation  $\tau$  and intra-event residuals are assumed to be normally distributed with zero mean and standard deviation  $\phi$ . The total standard deviation,  $\sigma$ , is computed as:

$$\sigma = \sqrt{\tau^2 + \phi^2} \quad (4)$$

## GMM FOR TEXAS, OKLAHOMA, AND KANSAS

To investigate the magnitude scaling adjustment, the inter-event residuals ( $\eta_i$ ) are plotted against the moment magnitude ( $M_w$ ) of each event in Figure 7 for four spectral periods ( $T = 0.1, 1.0, 3.0,$  and  $10$  s). Average values are shown for six magnitude bins along

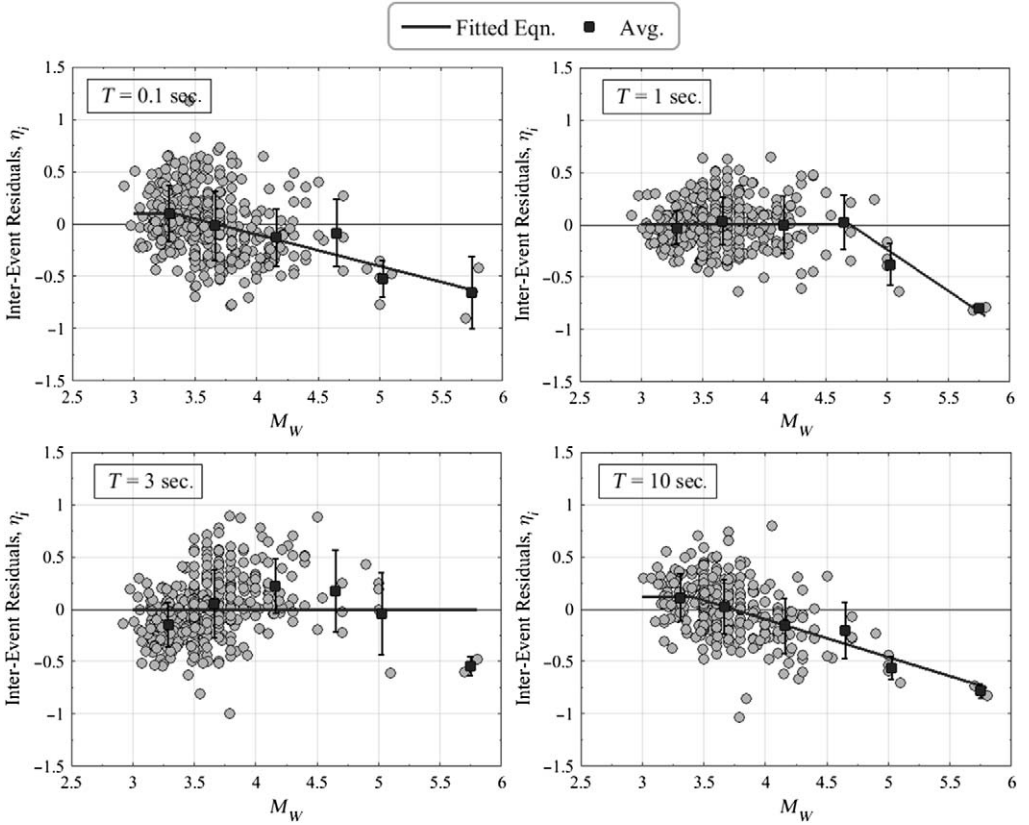


**Figure 7.** Inter-event residuals ( $\eta_i$ ) at four spectral periods ( $T = 0.1, 1.0, 3.0,$  and  $10$  s) versus  $M_w$ . Mean and  $\pm 1\sigma$  values are depicted for six magnitude bins (filled squares). The fitted model is also shown for reference (solid line).

with  $\pm 1$  standard deviation. Figure 7 shows that for larger magnitudes (i.e.,  $M_w > 4.5$ ) the inter-event residuals ( $\eta_i$ ) become strongly negative (i.e., the data are approximately 50% smaller than the HA15 model) for  $T = 0.1$  and  $1.0$  s. Although the data at  $M_w > 4.5$  are somewhat sparse, the residuals are large ( $\eta_i = -0.5$  to  $-1.0$ ) relative to the confidence intervals. At  $T = 3.0$  s, the data show a significantly different trend, with the residuals increasing with magnitude for  $M_w$  between 3 and 4.5, and then decreasing at larger magnitudes. Similar behavior is observed at periods between 2.5 to 5.0 s. At longer periods ( $T = 10$  s, Figure 7), the magnitude dependence of the inter-event residuals looks similar to the magnitude dependence at shorter periods. The trends in Figure 7 may be explained by differences in stress drop or other source parameters (i.e., mechanism). Some researchers have suggested that potentially induced earthquakes are associated with smaller stress drop values than natural earthquakes (e.g., Hough 2014), while other researchers have related smaller stress drop events with smaller focal depths (e.g., Yenier and Atkinson 2015). Regardless of the origin, smaller stress drops lead to weaker ground motions, which may explain the trends in Figure 7.

To adjust for the observed trends in the magnitude dependence of  $\eta_i$  (Figure 7), a hinged scaling factor ( $F_M$ ) is developed as follows:

$$F_M = \begin{cases} b_0, & 3.0 \leq M_w < M_b \\ b_0 + b_1(M_w - M_b), & M_b \leq M_w < 5.8 \end{cases} \quad (5)$$

where  $M_b$ ,  $b_0$ , and  $b_1$  are model coefficients (Table 2).  $F_M$  is only applicable for the magnitude range of the dataset  $3.0 \leq M_w \leq 5.8$  and should not be extrapolated outside of that range. The resulting  $F_M$  scaling relationships are shown in Figure 7 for the periods discussed. At periods 0.1, 1.0, and 10 s, the model captures the clear plateau at smaller magnitudes and largely negatively residuals at larger magnitudes, with the hinge magnitude ( $M_b$ ) varying with period. As noted earlier, the data at periods between 2.5 and 5.0 s show a significantly different trend. Because there is no physical explanation for this trend, no magnitude adjustment (i.e.,  $F_M = 0$ ) is incorporated at these periods.

After correcting the predictive residuals for the magnitude dependence of  $\eta_i$ , intra-event residuals ( $\varepsilon_{i,j}$ ) are used to examine regional differences in attenuation or site effects. Figure 8

**Table 2.** Model coefficients and standard deviations (in natural-log units)

Period (s)	$\alpha$	$R_b$	$M_b$	$b_0$	$b_1$	$c$	$V_c$	$C_{adj}$	$\tau$	$\phi$	$\sigma$
PGA	-0.6347	16.73	3.393	0.0908	-0.3217	0.4779	638.08	-0.22	0.30	0.54	0.62
PGV	-0.5339	13.94	2.925	0.2018	-0.2865	0.8682	515.96	0.18	0.27	0.51	0.58
0.05	-0.7112	18.20	3.403	0.0854	-0.3108	0.1668	945.85	-0.23	0.31	0.58	0.66
0.065	-0.6385	18.45	3.399	0.0880	-0.3166	0.3088	782.98	-0.14	0.31	0.58	0.66
0.08	-0.5478	19.21	3.398	0.0860	-0.3088	0.4052	686.43	-0.03	0.30	0.58	0.66
0.1	-0.4351	20.16	3.339	0.0986	-0.3019	0.5151	623.83	0.12	0.30	0.58	0.65
0.15	-0.4418	18.45	3.278	0.1135	-0.3032	0.5854	593.19	0.21	0.30	0.59	0.66
0.2	-0.4515	17.13	3.273	0.1138	-0.3009	0.6158	563.05	0.25	0.29	0.59	0.66
0.3	-0.4789	14.27	3.355	0.0998	-0.3011	0.6878	527.82	0.31	0.29	0.58	0.65
0.4	-0.5353	11.92	3.729	0.0643	-0.3655	0.8714	510.81	0.34	0.28	0.56	0.62
0.5	-0.6371	10.15	4.214	0.0244	-0.4728	0.9996	514.98	0.39	0.26	0.53	0.59
0.65	-0.7523	8.87	4.470	0.0094	-0.5887	1.0429	526.25	0.44	0.24	0.51	0.56
0.8	-0.7325	8.60	4.641	0.0083	-0.7468	1.0465	532.65	0.48	0.22	0.50	0.54
1	-0.6030	9.02	4.692	0.0078	-0.7923	1.0909	536.04	0.51	0.22	0.48	0.53
1.5	-0.5470	9.35	4.776	0.0059	-0.7244	1.0997	536.47	0.51	0.24	0.47	0.52
2	-0.4981	9.59	4.892	0.0056	-0.5086	1.1050	535.78	0.50	0.25	0.46	0.53
2.5	-0.4738	9.63	5.800	0.0000	0.0000	1.1049	533.45	0.48	0.28	0.45	0.53
3	-0.4847	9.46	5.800	0.0000	0.0000	1.0961	530.31	0.47	0.29	0.45	0.54
3.5	-0.5269	9.21	5.800	0.0000	0.0000	1.0770	527.37	0.45	0.30	0.45	0.54
4	-0.5844	9.06	5.800	0.0000	0.0000	1.0462	525.63	0.43	0.30	0.46	0.55
5	-0.6766	9.45	5.800	0.0000	0.0000	0.9561	525.14	0.40	0.27	0.47	0.54
6	-0.6983	10.36	4.507	0.0042	-0.1059	0.8507	525.48	0.37	0.24	0.46	0.52
7.5	-0.6760	11.03	3.633	0.0505	-0.1954	0.7043	524.83	0.36	0.23	0.45	0.51
10	-0.7138	11.39	3.400	0.1218	-0.3627	0.5605	524.53	0.40	0.22	0.46	0.51

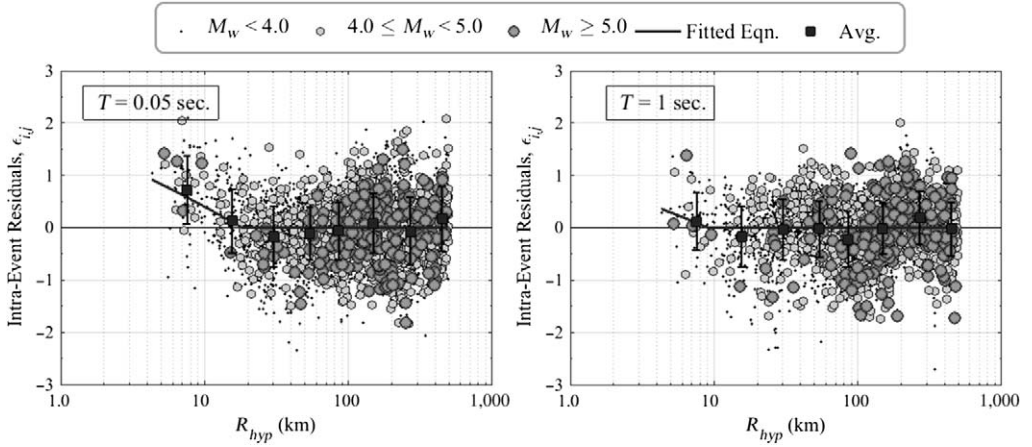


**Figure 8.** Intra-event residuals ( $\epsilon_{i,j}$ ) at two spectral periods ( $T = 0.05$  and  $1.0$  s) versus hypocentral distance ( $R_{hyp}$ ). Data are separated based on three magnitude bins. Mean and  $\pm 1\sigma$  are depicted for eight log-spaced distance bins (filled squares). The fitted model is also shown for reference (solid line).

shows the intra-event residuals ( $\epsilon_{i,j}$ ) as a function of hypocentral distance for spectral accelerations at  $T = 0.05$  and  $1.0$  s. These data show residuals close to zero at  $R_{hyp}$  greater than about 15–20 km, indicating that the overall anelastic attenuation and geometrical spreading characteristics at these distances are similar to those modeled by HA15 for natural seismicity in CENA. Nonetheless, at  $R_{hyp} < 20$  km positive residuals are observed, indicating the recorded motions are larger than predicted by the HA15 model. This effect is more pronounced at shorter periods but is still observed at longer periods (e.g.,  $T = 1.0$  s). The larger recorded motions at short distances can possibly be attributed to the generally shallower focal depths of the events in Texas, Oklahoma, and Kansas with respect to the natural seismicity in CENA. To correct for the observed differences in near source attenuation (Figure 8), a distance scaling term  $F_R$  is defined as a hinged function:

$$F_R = \begin{cases} \alpha \cdot \ln\left(\frac{4\text{km}}{R_b}\right), & R_{hyp} < 4 \text{ km} \\ \alpha \cdot \ln\left(\frac{R_{hyp}}{R_b}\right), & 4 \text{ km} \leq R_{hyp} < R_b \\ 0, & R_{hyp} \geq R_b \end{cases} \quad (6)$$

where  $R_b$  is the transition distance beyond which no adjustment is needed,  $\alpha$  is a model coefficient, and  $R_{hyp}$  is hypocentral distance. To avoid unrealistic ground motion amplitudes at small  $R_{hyp}$ , the  $F_R$  function is forced to saturate at  $R_{hyp} < 4$  km, the smallest  $R_{hyp}$  in the database. The resulting fits to the residuals at periods 0.05 and 1.0 s are shown in Figure 8.

The intra-event residuals ( $\epsilon_{i,j}$ ) are plotted against the site parameter  $V_{S30}$  in Figure 9 and show an obvious trend toward strongly negative residuals (i.e., overprediction) at  $V_{S30}$  values smaller than about 500–600 m/s. For soft sites ( $V_{S30} < 200$  m/s), the recordings indicate

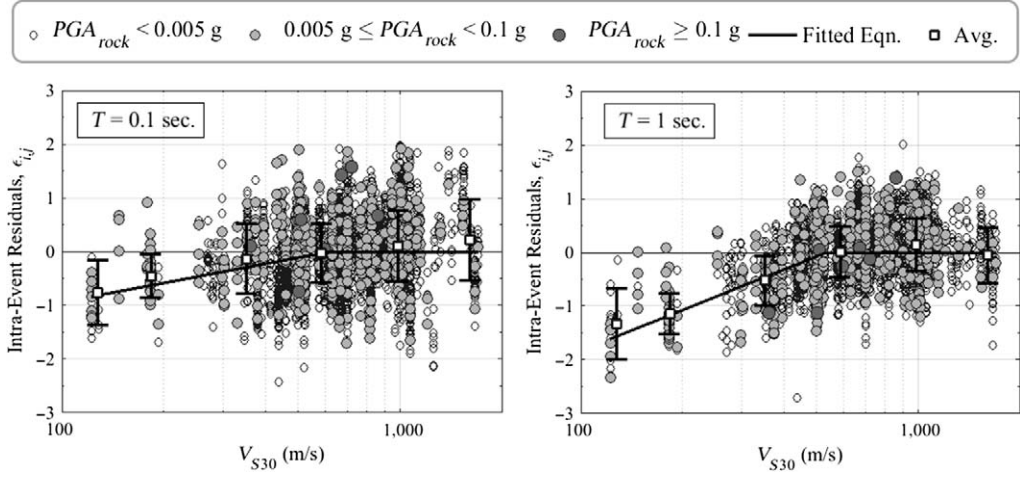


**Figure 9.** Intra-event residuals ( $\epsilon_{i,j}$ ) at two spectral periods ( $T = 0.1$  and  $1.0$  s) versus  $V_{S30}$ . Data are separated based on four  $PGA_{rock}$  bins. Mean and  $\pm 1\sigma$  values are depicted for six  $V_{S30}$  bins (filled squares). The fitted model is also shown for reference (solid line).

motions 40% smaller than predicted by the HA15 model at  $T = 0.1$  s, while the observations are almost 70% smaller at  $T = 1.0$  s. The discrepancies between the HA15 model and recordings at softer sites in Texas, Oklahoma, and Kansas are likely due to the fact that HA15 utilizes the BSSA14 WNA site amplification model. As discussed in [Zalachoris et al. \(2017\)](#), the depth to rock (i.e.,  $V_{S30} > 760$  m/s) in Texas, Oklahoma, and Kansas tends to be small even at sites with small  $V_{S30}$ . In WNA, sites with small  $V_{S30}$  typically are characterized by deeper sediments that generate larger amplification, particularly at longer periods. It should be noted that the data in Figure 9 have been binned based on four levels of PGA, as computed at a reference condition of  $V_{S30} = 760$  m/s ( $PGA_{rock}$ ). Because the vast majority of the computed residuals correspond to values of  $PGA_{rock} < 0.05$  g, the observed difference in  $V_{S30}$  scaling represents only the linear-elastic component of site amplification.

To correct for the observed differences in site amplification (Figure 9), a site effects scaling factor  $F_S$  is defined as a function of  $V_{S30}$  as follows:

$$F_S = \begin{cases} c \cdot \ln\left(\frac{V_{S30}}{V_c}\right) & V_{S30} < V_c \\ 0 & V_{S30} \geq V_c \end{cases} \quad (7)$$

where  $V_c$  is the limiting velocity above which site amplification adjustment is not needed, and  $c$  is a model coefficient. The resulting fits to the residuals for  $T = 0.1$  and  $1.0$  s are shown in Figure 9.

To illustrate the revised site amplification model, which represents an adjustment to the BSSA14 site amplification model using Equation 7, Figure 10 compares the linear-elastic  $V_{S30}$  scaling developed in this study with the BSSA14 site amplification model used by

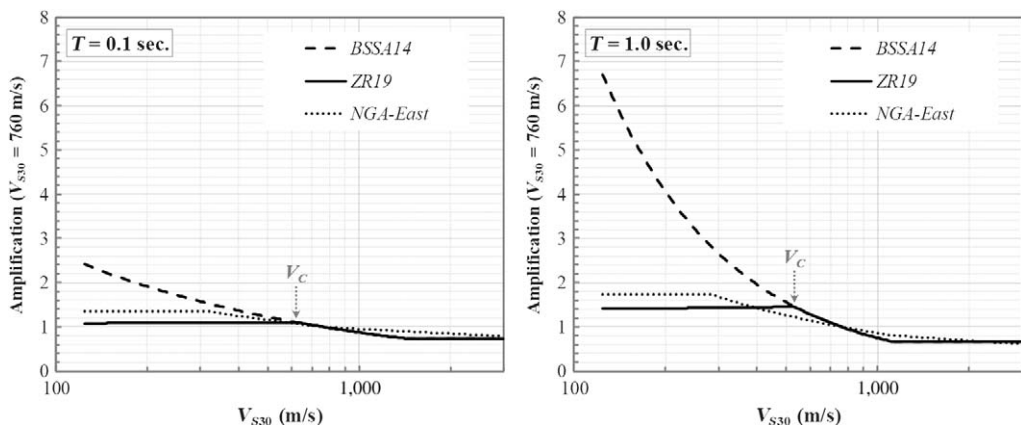


**Figure 10.** Comparison between the linear site amplification models of Boore et al. (2014; BSSA14), adjusted model of the present study (ZR19), and model developed by NGA-East (Stewart et al. 2017).

HA15. The  $V_{S30}$  scaling is shown relative to a reference site condition of  $V_{S30} = 760$  m/s and for periods of 0.1 and 1.0 s. For  $V_{S30} < V_c$ , the site amplification model from this study (labeled ZR19) provides a flatter, and substantially smaller, response than BSSA14, which is most likely due to the relatively shallower depth to bedrock in the study region (Zalachoris et al. 2017) in comparison to WNA. This difference is more pronounced for longer periods, with the new model predicting site amplification values approximately one-fourth of the values predicted by BSSA14 at smaller  $V_{S30}$ . Also shown in Figure 10 is the linear-elastic site amplification model proposed for CENA as part of the NGA-East project (Stewart et al. 2017). This NGA-East site amplification model exhibits similar trends to the one developed in this study, with smaller site amplification for softer soil conditions, particularly at longer periods.

The final parameter in the model is  $C_{adj}$ , the factor that adjusts the overall level of the HA15 model relative to the regional data. The values of  $C_{adj}$  are plotted versus period in Figure 11. The  $C_{adj}$  values are about  $-0.2$  at short periods, become 0 at  $T = 0.08$  s, and increase to 0.5 at longer periods. These values are consistent with the original overall residuals displayed in Figure 6. On average, across all distances, negative residuals are shown in Figure 6 for PGA; the average residuals are slightly positive for  $T = 0.1$  s, and they become more positive at  $T = 1$  and 3 s. The  $C_{adj}$  factor accounts for all the regional source/path/site effects that are not captured by the other parts of the model, and thus it is difficult to develop physical explanations for the values in Figure 11.

Table 2 presents the computed model coefficients for PGA, PGV, and selected spectral periods between 0.05 and 10 s. A complete list of computed model coefficients at 51 spectral periods is provided in the online appendix. As noted earlier, statistical  $p$ -values were computed for each model parameter. Most of the model parameters have  $p$ -values significantly smaller than 0.05, with two exceptions. The  $F_M$  parameter  $b_0$ , which represents the magnitude adjustment below the hinge magnitude, displays  $p$ -values between 0.1 and 0.2 for

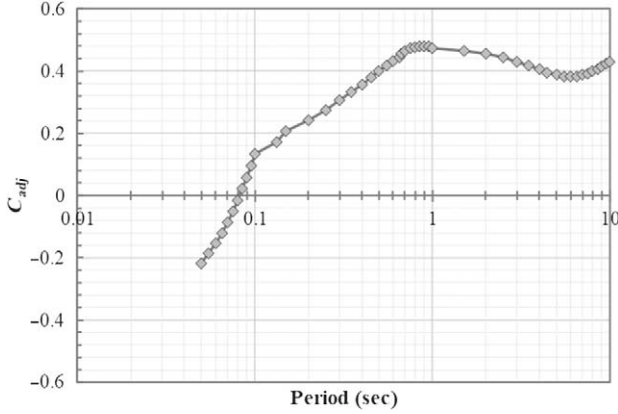


**Figure 11.** Overall adjustment factor  $C_{adj}$  as a function of period.

periods between 0.75 and 7.5 s. The  $F_R$  parameter  $R_b$ , which is the distance below which the distance adjustment occurs, displays  $p$ -values between 0.05 and 0.1 at periods between 0.5 and 5.0 s and between 9 and 10 s. These larger  $p$ -values indicate more uncertainty in these parameters than the other parameters.

The adjusted ground motion predictions applicable for small-to-moderate earthquake events in Texas, Oklahoma, and Kansas ( $IM_{TX-OK-KS}$ ) are obtained as follows:

$$IM_{TX-OK-KS} = F \cdot IM_{HA15} \quad (8)$$

where  $F$  is given by Equations 3–7 and  $IM_{HA15}$  is the ground motion parameter value predicted by the Hassani and Atkinson (2015) CENA GMM. Given the data limits used to develop the model in this study, Equation 8 should only be used for  $M_w = 3–5.8$  and  $R_{hyp} < 500$  km.

The standard deviation values (i.e.,  $\tau$ ,  $\phi$ , and  $\sigma$  in natural-log units) of the developed model are also listed in Table 2. The total standard deviation ( $\sigma$ ) is on the order of 0.55–0.7 and is largest at shorter periods. The total standard deviation is dominated by the intra-event component ( $\phi$ ), which takes on values between 0.45–0.6. The inter-event standard deviation ( $\tau$ ) varies between 0.2–0.3. The increase in standard deviation at shorter periods can possibly be attributed to variations in the source stress parameter for small  $M$  earthquakes (Boore at al. 2014), since the ground motion database of this study includes both mainshock and aftershock events, particularly for  $M_w < 4.5$ .

Figure 12 illustrates a comparison between the observed data in Texas, Oklahoma, and Kansas for events with  $M_w > 5.0$  and the predictive relationship developed in this study, denoted ZR19. Predictions are shown for  $M_w = 5.3$ , the average magnitude of the data shown. The HA15 reference CENA GMM as well as the small-magnitude, short-distance Atkinson (2015, APIE15) GMM are also shown. The APIE relationship is only plotted for  $R_{hyp} < 40$  km because that is its limit of applicability. The observed data have been corrected to a reference site condition of  $V_{S30} = 760$  m/s using the revised  $V_{S30}$  scaling

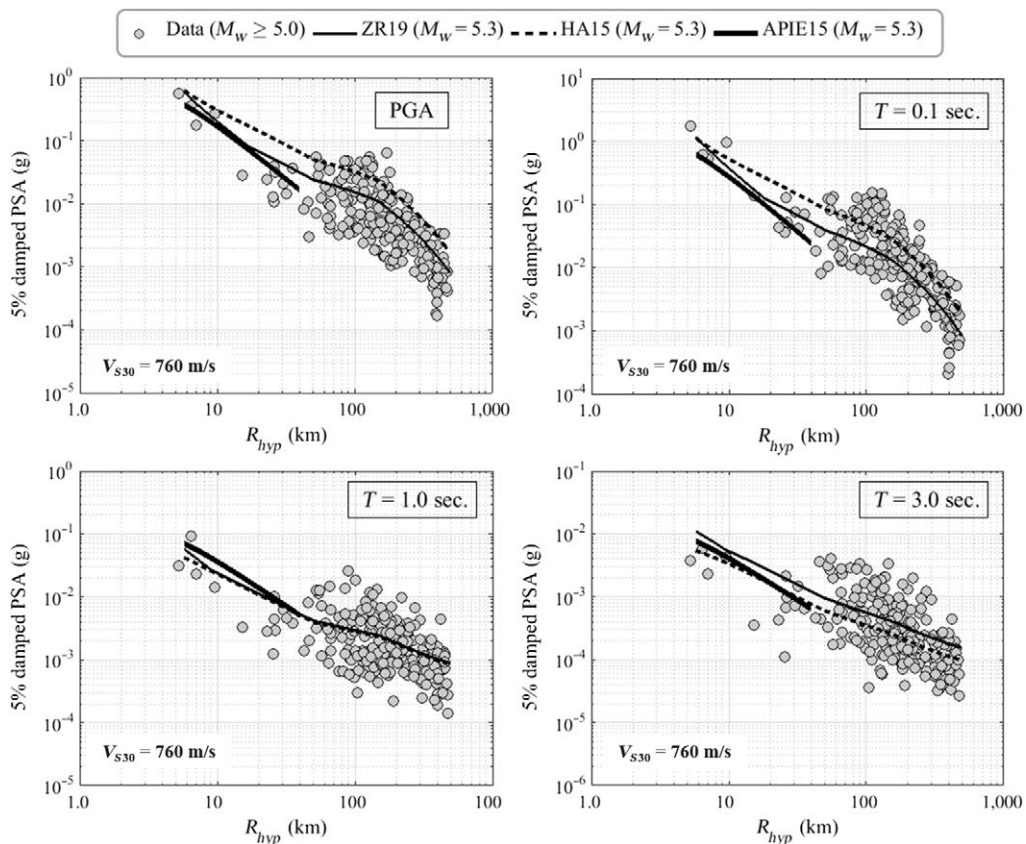


**Figure 12.** Comparison of the observed data for  $M_w > 5.0$  with the CENA Hassani and Atkinson (2015) GMPE (HA15), the small-magnitude Atkinson (2015) GMPE (APIE15), and the adjusted model of the present study (ZR19) for reference site conditions ( $V_{S30} = 760$  m/s).

developed in this study. As seen in Figure 12, the ZR19 model matches the observations at all distances and spectral periods, as expected. For PGA and  $T = 0.1$  s, ZR19 predicts smaller motions than HA15 because of the strong  $F_M$  magnitude correction at shorter periods. As  $R_{hyp}$  approaches 5 km, ZR19 and HA15 predict similar levels of shaking at these periods because of the  $F_R$  distance correction (Equation 6) incorporated in this study. At  $T = 1.0$  s, ZR19 predicts motions very similar to HA15, while at  $T = 3.0$  s, ZR19 predicts motions larger than HA15. Across all the periods shown in Figure 12, the small-magnitude APIE15 model provides predictions most similar to ZR19 for  $R_{hyp}$  up to 40 km.

Figure 13 compares the response spectra produced using the HA15 and ZR19 models for  $M_w = 5.0$  and hypocentral distances of 5 and 20 km. Two site conditions are considered,  $V_{S30} = 760$  and 200 m/s. For  $V_{S30} = 760$  m/s (Figure 13a), ZR19 provides larger spectral accelerations than HA15 for  $R_{hyp} = 5$  km because of the revised near-source distance scaling

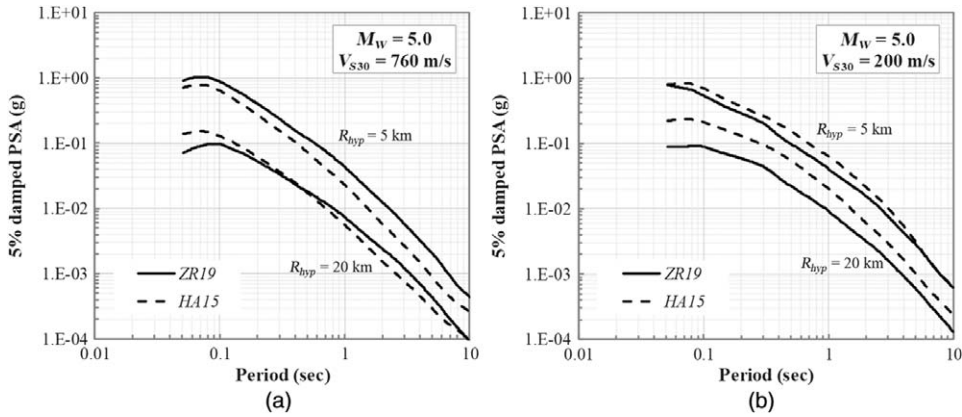


**Figure 13.** Acceleration response spectra for  $M_w = 5.0$ ,  $R_{hyp} = 5$  km, and  $R_{hyp} = 20$  km, and (a)  $V_{S30} = 760$  m/s and (b)  $V_{S30} = 200$  m/s.

from Equation 6. For  $R_{hyp} = 20$  km, ZR19 predicts smaller spectral accelerations at  $T < 0.4$  s and larger values at  $T > 0.4$  s. For  $V_{S30} = 200$  m/s (Figure 13b), ZR19 predicts smaller spectral accelerations than HA15 at  $R_{hyp} = 20$  km because of the weaker  $V_{S30}$  scaling included in ZR19 (Figure 10). At  $R_{hyp} = 5$  km, ZR19 predicts spectral accelerations similar to HA15 because of the increased near-source distance scaling in ZR19 balancing out its smaller  $V_{S30}$  scaling.

## DISCUSSION AND CONCLUSIONS

In this study, recorded earthquake ground motions are used to develop a GMM to predict ground shaking for the observed, and potentially induced, seismicity in Texas, Oklahoma, and Kansas. A ground motion database was developed that includes 4,528 recordings from 376 events and 213 seismic stations. The ground motion data cover a magnitude range of  $3.0 \leq M_w < 5.8$  and a distance range of  $R_{hyp} < 500$  km; thus this is the range of applicability of the model. The  $V_{S30}$  for the stations were assigned predominantly using the  $P$ -wave seismogram method (Zalachoris et al. 2017) or through recent geologic proxies for Texas, Oklahoma, and Kansas (Table 1; Cox et al. 2017).

The GMM is developed using the referenced empirical approach, which involves empirical modification of a reference GMM. For this study, the Hassani and Atkinson (2015) CENA GMM is selected as the reference GMM. Using the developed ground motion database and the HA2015 GMM, residuals (in natural-log units) between the ground motion observations and predictions were computed. The residuals were partitioned between inter-event and intra-event residuals through a mixed effects regression, and these residuals were used to identify adjustments with respect to magnitude, distance, and  $V_{S30}$ .

The resulting GMM predicts smaller ground motions than the HA15 reference GMM at periods less than about 1.0 s for larger magnitudes. The developed GMM predicts increased ground motions at short distances ( $R_{hyp} \leq 20$  km), which is likely due to the smaller focal depths of the events in Texas, Oklahoma, and Kansas. This effect is observed at all periods

but is largest (i.e., more than a factor of 2) at  $T$  less than about 0.1 s. The  $V_{S30}$  scaling for the newly developed model is weaker than for the HA15 model, with less amplification at  $V_{S30} < 600$  m/s. This effect is most pronounced at longer periods.

The GMM developed in this study accounts for important region-specific features of the earthquake events and geology in Texas, Oklahoma, and Kansas. The earthquake events used in this study have a median focal depth of 5 km, and this smaller focal depth can result in smaller stress drops. These smaller stress drops can lead to smaller motions, particularly for larger magnitude events. The smaller focal depths also affect the near-source distance scaling, such that motions at shorter distances are more intense. Finally, the geology of Texas, Oklahoma, and Kansas (outside of the Gulf Coast region) is generally characterized with soil of moderate depth (Zalachoris et al. 2017), such that even sites with small  $V_{S30}$  do not have significant soil thickness. These characteristics lead to weaker  $V_{S30}$  scaling and smaller site amplification.

## ACKNOWLEDGMENTS

This work was sponsored through funding from the State of Texas through the TexNet Seismic Monitoring Project from the Industrial Associates of the Center for Integrated Seismic Research (CISR) at the Bureau of Economic Geology of the University of Texas. This funding is gratefully acknowledged.

## APPENDICES

Please refer to the online version of this manuscript to access the supplementary material provided in the Appendices.

## REFERENCES

- Abrahamson, N. A., and Youngs, R. R., 1992. A stable algorithm for regression analyses using the random effects model, *Bulletin of the Seismological Society of America* **82**, 505–510.
- Atkinson, G. M., 2008. Ground-motion prediction equations for eastern North America from a referenced empirical approach: Implications for epistemic uncertainty, *Bulletin of the Seismological Society of America* **98**, 1304–1318.
- Atkinson, G. M., 2015. Ground-motion prediction equation for small-to-moderate events at short hypocentral distances, with application to induced-seismicity hazards, *Bulletin of the Seismological Society of America* **105**, 981–992.
- Atkinson, G. M., and Mahani, A. B., 2013. Estimation of moment magnitude from ground motions at regional distances, *Bulletin of the Seismological Society of America* **103**, 107–116.
- Atkinson, G. M., Greig, D. W., and Yenier, E., 2014. Estimation of moment magnitude ( $M$ ) for small events ( $M < 4$ ) on local networks, *Seismological Research Letters* **85**, 1116–1124.
- Bommer, J. J., Dost, B., Edwards, B., Stafford, P. J., van Elk, J., Doornhof, D., and Ntinalexis, M., 2016. Developing an application-specific ground-motion model for induced seismicity, *Bulletin of the Seismological Society of America* **106**, 158–173.
- Boore, D. M., 2010. Orientation-independent, nongeometric-mean measures of seismic intensity from two horizontal components of motion, *Bulletin of the Seismological Society of America* **100**, 1830–1835.

- Boore, D. M., Stewart, J. P., Seyhan, E., and Atkinson, G. M., 2014. NGA-West2 equations for predicting PGA, PGV, and 5% damped PSA for shallow crustal earthquakes, *Earthquake Spectra* **30**, 1057–1085.
- Cox, B., Rathje, E., Paine, J., Cheng, T., Yust, M., and Zalachoris, G., 2017. Task 4 Tech Memo: V<sub>S30</sub> Map. Project 0-6916: Seismic Vulnerability and Post-Event Actions, Center for Transportation Research at the University of Texas at Austin, 23 p.
- Douglas, J., Edwards, B., Convertito, V., Sharma, N., Tramelli, A., Kraaijpoel, D., Mena Cabrera, B., Maercklin, N., and Troise, C., 2013. Predicting ground motion from induced earthquakes in geothermal areas, *Bulletin of the Seismological Society of America* **103**(3), 1875–1897.
- Ellsworth, W. L., 2013. Injection-induced earthquakes, *Science* **341**(6142), 1225942.
- Goulet, C. A., Kishida, T., Ancheta, T. D., Cramer, C. H., Darragh, R. B., Silva, W. J., Hashash, Y. M. A., Harmon, J., Stewart, J. P., Wooddell, K. E., and Youngs, R. R., 2014. *PEER NGA-East Database, PEER Report 2014/17*, Pacific Earthquake Engineering Research Center, Berkeley, CA.
- Hassani, B., and Atkinson, G. M., 2015. Referenced empirical ground-motion model for eastern North America, *Seismological Research Letters* **86**, 477–491.
- Hough, S. E., 2014. Shaking from injection-induced earthquakes in the Central and Eastern United States, *Bulletin of the Seismological Society of America* **104**, 2619–2626.
- Incorporated Research Institutions for Seismology (IRIS), 2018. IRIS Data Management Center, available at <https://www.iris.edu/hq/> (last accessed 1 July 2018).
- Kim, B., Hashash, Y. M. A., Rathje, E. M., Stewart, J. P., Ni, S., Somerville, P. G., Kottke, A. R., Silva, W. J., and Campbell, K. W., 2016. Subsurface shear wave velocity characterization using P-wave seismograms in Central and Eastern North America, *Earthquake Spectra* **32**, 143–169.
- Ni, S., Li, Z., and Somerville, P., 2014. Estimating subsurface shear velocity with radial to vertical ratio of local P waves, *Seismological Research Letters* **85**, 82–90.
- Pacific Earthquake Engineering Research Center (PEER), 2015. *NGA-East: Median Ground-Motion Models for the Central and Eastern North America Region, PEER Report 2015/04*, PEER, Berkeley, CA.
- Petersen, M. D., Mueller, C. S., Moschetti, M. P., Hoover, S. M., Llenos, A. L., Ellsworth, W. L., Michael, A. J., Rubinstein, J. L., McGarr, A. F., and Rukstales, K. S., 2016. *2016 One-Year Seismic Hazard Forecast for the Central and Eastern United States from Induced and Natural Earthquakes, Open-File Report 2016-1035*, U.S. Geological Survey, Reston, VA.
- Stewart, J. P., Parker, G. A., Harmon, J. A., Atkinson, G. M., Boore, D. M., Darragh, R. B., Silva, W. J., and Hashash, Y. M. A., 2017. *Expert Panel Recommendations for Ergodic Site Amplification in Central and Eastern North America, PEER Report 2017/04*, Pacific Earthquake Engineering Research Center, Berkeley, CA.
- Yenier, E., and Atkinson, G. 2015. Regionally adjustable generic ground-motion prediction equation based on equivalent point-source simulations: Application to Central and Eastern North America, *Bulletin of the Seismological Society of America* **105**, 1989–2009.
- Yong, A., Thompson, E. M., Wald, D., Knudsen, K. L., Odum, J. K., Stephenson, W. J., and Haefner, S., 2015. Compilation of V<sub>S30</sub> data for the United States, *U.S. Geological Survey Data Series 978*, Reston, VA.
- Zalachoris, G., Rathje, E. M., and Paine, J. G., 2017. VS30 characterization of Texas, Oklahoma, and Kansas using the P-wave seismogram method, *Earthquake Spectra* **33**, 943–961.

(Received 26 February 2018; Accepted 29 August 2018)